

Flexible Timbo-Like Triboelectric Nanogenerator as Self-Powered Force and Bend Sensor for Wireless and Distributed Landslide Monitoring

Zhiwei Lin, Qiang He, Yang Xiao, Tao Zhu, Jun Yang, Chenchen Sun, Zhihao Zhou, Heng Zhang, Ziying Shen, Jin Yang,* and Zhong Lin Wang*

As worldwide landslides frequently result in enormous casualties and huge economic losses, new landslide monitoring technologies are urgently required to develop for preventing and mitigating landslide hazard. In this paper, a self-powered, flexible, timbo-like triboelectric force and bend sensor (TTEFBS) is proposed and implemented, with the aim of effectively monitoring landslides. The fabricated TTEFBS, based on a single-electrode working mode, consists of a timbo-like inner polydimethylsiloxane (PDMS) core coated with a carbon electrode and an outer silicon rubber tube. Owing to the novel structure and sensing mechanism, the TTEFBS achieves high sensitivities (5.20 V N^{-1} under pressing and 1.61 V rad^{-1} under bending), fast response/relaxation time ($<6 \text{ ms}$), and long-term stability/reliability (more than 40 000 cycles). Furthermore, a wireless and distributed monitoring system using an array of TTEFBSs is developed for systematically detecting rockfalls, deep-seated landslides, and superficial landslides. Additionally, a zigzag-structured triboelectric nanogenerator (Z-TENG), characterized by an open-circuit voltage of $\approx 2058 \text{ V}$ and a short-circuit current of $\approx 154 \mu\text{A}$, is successfully fabricated for scavenging energy from moving cars to provide power in wild environments, thereby forming a self-powered monitoring system. This work may further inspire rapid progress of TENG in applications of wireless, distributed sensing, and environmental/infrastructure monitoring.

large numbers of casualties, huge economic losses, and severe damages to structures and infrastructures.^[1,2] In general, the landslide is a form of mass wasting that includes a wide range of ground movements, such as rockfalls, deep-seated slope failures, and superficial landslides, which needs to be monitored at all times. Conventional methods, including geomorphological field mapping,^[3] visual interpretation of stereoscopic aerial photographs,^[4] triangulation,^[5] and electronic distance measurement (EDM)^[6] have been investigated for mapping landslides and monitoring slope instabilities. Unfortunately, these methods are time-consuming and resource-intensive.^[7,8] At present, multiple approaches based on satellite, airborne, and terrestrial remote sensing technologies have been researched extensively, promising to reduce the time and resources required for compilation and systematic update.^[7,9] Nevertheless, underlying problems such as vegetation overgrowth and night-capturing restrictions make it difficult to monitor from optical images and cause false alarm incidents,


thus limiting their utilization.^[10] Furthermore, subsurface landslides are difficult to identify using standard aerial photography or satellite imaging.^[7,10,11] To monitor subsurface landslides, other technologies, such as electrical resistivity tomography

1. Introduction

As one of the three major global geological disasters, along with earthquakes and volcanic eruptions, landslides have caused

Dr. Z. Lin, Dr. Q. He, Prof. T. Zhu, C. Sun, Dr. Z. Zhou, H. Zhang, Z. Shen, Prof. J. Yang
Department of Optoelectronic Engineering
Key Laboratory of Optoelectronic Technology and Systems
Ministry of Education
Chongqing University
Chongqing 400044, China
E-mail: yangjin@cqu.edu.cn

Dr. Y. Xiao
Department of Civil Engineering
Chongqing University
Chongqing 400044, China

 The ORCID identification number(s) for the author(s) of this article can be found under <https://doi.org/10.1002/admt.201800144>.

Dr. J. Yang
Chongqing Institute of Green and Intelligent Technology
Chinese Academy of Sciences
Chongqing 400714, China

Prof. Z. L. Wang
School of Materials Science and Engineering
Georgia Institute of Technology
Atlanta, GA 30332, USA
E-mail: zlwang@gatech.edu

Prof. Z. L. Wang
Beijing Institute of Nanoenergy and Nanosystems
Chinese Academy of Sciences
Beijing 100083, China

DOI: 10.1002/admt.201800144

(ERT), ground-penetrating radar (GPR), and distributed optical fiber sensors (DOFS), have been investigated. However, key limitations on the use of these technologies are the cost and complexity of the monitoring system and the requirement of external power sources.^[12–14] Therefore, the research for self-powered, effective, and real-time landslide monitoring is still an urgent challenge, which needs to be conquered.

Recently, the triboelectric nanogenerator (TENG), based on triboelectrification and electrostatic induction, was first reported by Wang and co-workers in 2012^[15]; this can produce high electrical output in response to an external mechanical excitation, and thus bring about emerging techniques.^[16] Because of the advantages of high output, high energy conversion efficiency and inexpensive fabrication, TENGs have been used successfully for harvesting energy, such as from vibrations,^[17–24] acoustics,^[25,26] wind,^[27–29] water,^[30–36] and biomechanical.^[37–41] Furthermore, TENGs show great potential for applications as self-powered sensors. For instance, TENGs have been developed as self-powered sensors for detecting water/ethanol,^[42] wind speed sensing,^[43] microliquid biological and chemical sensing,^[44] and vibration monitoring.^[45] It is worth mentioning that, by comparison with other fundamental working modes, in the single-electrode mode one triboelectric layer can move freely without any restriction.^[16] With this advantage, the single-electrode mode is particularly suitable for acting as a self-powered sensor for detecting any electrically charged object.^[46] This mode has been reported widely in self-powered sensor applications, such as pressure/touch sensors and human motion sensors in human health monitoring,^[47–50] acceleration sensor in vibration monitoring,^[51] and self-powered identification systems.^[52] Nevertheless, landslide monitoring is a major application that has not been realized for TENGs.

Herein, a self-powered sensing and monitoring system based on a timbo-like triboelectric force and bend sensor (TTEFBS) is proposed as an attractive alternative to the landslide monitoring system. Because of this promising design, a superior performance is achieved, including high sensitivities of 5.20 V N⁻¹ under pressing and 1.61 V rad⁻¹ under bending, fast response/relaxation time of <6 ms, and long-term stability/reliability measurements for 40 000 cycles. Multiple TTEFBSs are integrated into an array for rockfall detection and slope monitoring. Furthermore, to establish a self-powered monitoring system, we fabricated a zigzag-structured triboelectric nanogenerator (Z-TENG) in a deceleration strip as a power source for scavenging energy from moving cars on roads. This work marks an important progress toward the practical application of TENG in environmental/infrastructure monitoring.

2. Results and Discussion

The structure of the TTEFBS is depicted schematically in Figure 1a. The polydimethylsiloxane (PDMS) core is molded with a timbo-like structure through the injection molding technology (Figure S1, Supporting Information). The shape of its cross-section is inspired from the petal, enabling the TTEFBS to respond to the external dynamic force with high sensitivity. A carbon layer is deposited on the outer surface of the flexible PDMS core as an electrode; the entire inner core is then

suitably assembled in a silicon rubber tube. Figure 1b-i is the photograph of the flexible inner core. Figure 1b-ii shows a scanning electron microscopy (SEM) image of the surface morphology of the inner core, in which the microstructures tend to be randomly distributed. These microstructures are likely to be readily deformed and become adaptive to the surface morphology of the silicon rubber for an intimate contact. The photograph of the fabricated TTEFBS in Figure 1c illustrates the flexibility of the sensor.

The TTEFBS is based on the coupling effect of contact electrification and electrostatic induction and works in single-electrode mode. Figure 1d–e present the working mechanism of the single-electrode TTEFBS under short-circuit condition and the numerically calculated potential distribution under open-circuit condition, respectively. When the TTEFBS is compressed or bent, the carbon electrode and the outer silicon rubber tube are brought into adequate contact by an external force, and the electrons are injected from the inner carbon layer into the silicon rubber layer because of the difference in surface electron affinities (Figure 1d-i). The induced charges are balanced because of electrostatic induction; hence, there is neither charge flow nor potential difference across the carbon electrode and outer tube, nor between the electrode and the ground (Figure 1e-i). Under a short-circuit condition, electrons will be driven from the ground to the carbon electrode under releasing, while from the carbon electrode to the ground under pressing, to balance the electric potential (Figure 1d-ii). Once the contact area decreases under releasing or increases under pressing, the immediate charge separation will induce a positive potential on the electrode relative to the ground under open-circuit conditions (Figure 1e-ii). The full cycle of the electricity generation process for the TTEFBS can be seen in Figures S2 and S3 in the Supporting Information.

The typical electrical responses of the TTEFBS under external mechanical stimulation by a mechanical shaker are shown in Figure 1f–g. As a 2 Hz cyclic pressing force (40.0 N) is applied on the TTEFBS with eight petals, it produces an open-circuit voltage (V_{OC}) of ≈ 32.2 V and a short-circuit current (I_{SC}) of ≈ 1.15 μ A. The V_{OC} increases when the pressing force is applied on the sensor, and decreases under the releasing force (Figure 1f). Furthermore, it can be seen that the I_{SC} is pulse-like. A negative peak of I_{SC} is observed once the TTEFBS is pressed; while the peak of I_{SC} becomes positive at the moment of the releasing force (Figure 1g), which agrees with the aforementioned analyzed electricity generation process.

To investigate the effect of the petal numbers on the output performances, the TTEFBSs with four, eight, and twelve petals were tested under various pressing forces/bending angles with a constant frequency of 2 Hz. The experimental setup is illustrated in Figure S4 in the Supporting Information. First, the electrical outputs were measured with different pressing forces. In Figure 2a, x and y are the pressing directions. The direction x is along AO, while the direction y is the angular bisector BO of adjacent petals. The voltage-force curves of the TTEFBSs with different petal numbers in the same pressing direction x are plotted in Figure 2b. It is worth noting that the three TTEFBSs show the two-region behavior; that is, high sensitivity in a low-force region and low sensitivity in a high-force region. In the low-force region, the increased force results in

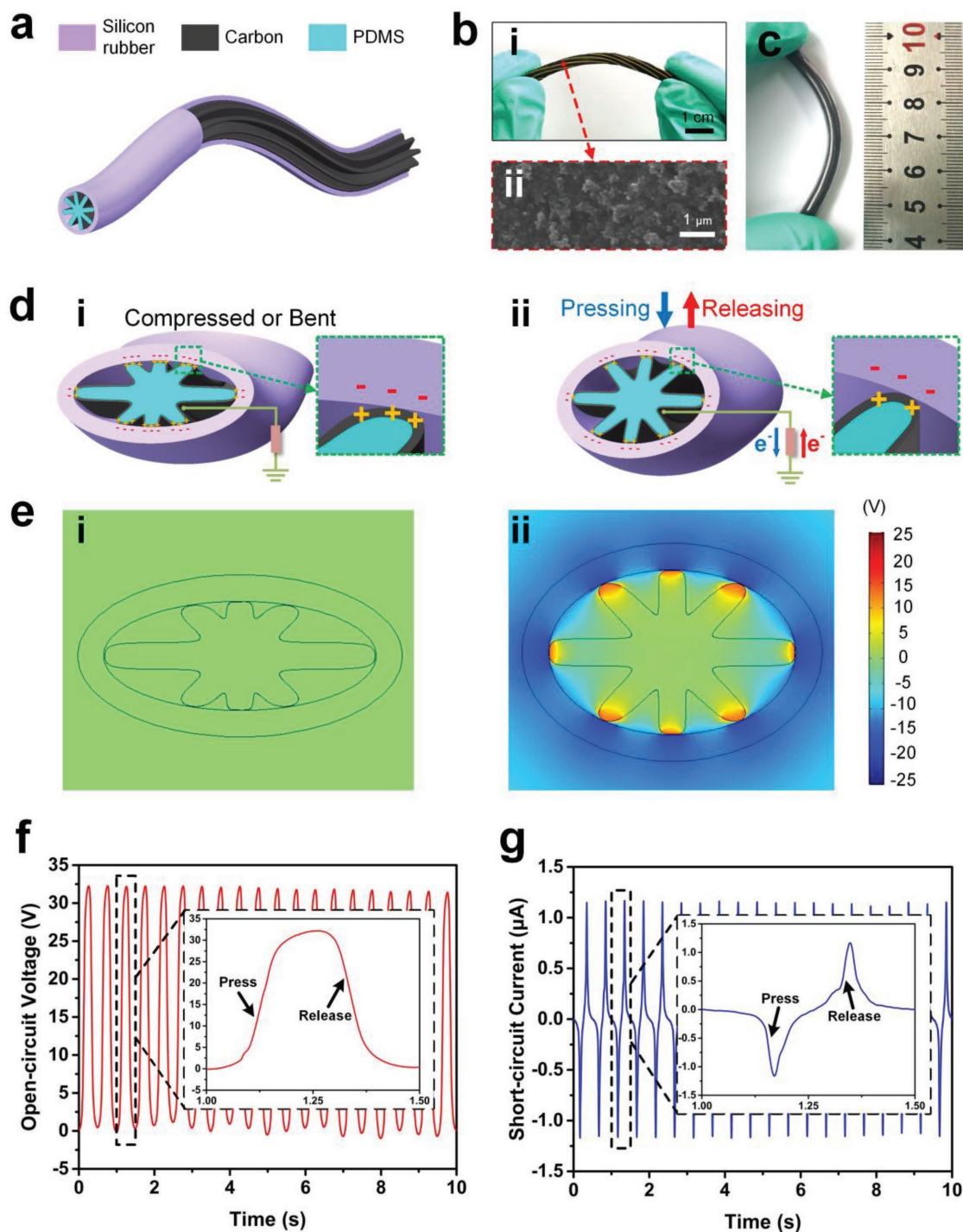


Figure 1. Structure, working mechanism, and typical electrical responses of the TTEFBS. a) Schematic illustrations of TTEFBS. b-i) Photograph of the inner core (scale bar, 1 cm. The petals are highlighted in orange lines.) and b-ii) SEM image of carbon-coated surface of PDMS (scale bar, 1 μm). c) Photograph of an as-fabricated TTEFBS. d) Working mechanism of TTEFBS and e) numerical calculations of the potential on TTEFBS electrodes at two typical states, as evaluated by COMSOL. Measured typical electrical responses, including f) open-circuit voltage and g) short-circuit current of the TTEFBS.

a drastic contact area change, leading to a larger voltage variation, whereas in the high-force region, an equal change in force results in a smaller change in contact area.^[48] Note that the TTEFBS with twelve petals has the highest sensitivity which

is caused by the largest contact area. Relying on the novel working principle and the unusual timbo-like structure allows the TTEFBS with twelve petals to distinguish itself in terms of sensitivity together with linear range of force (5.20 V N^{-1} in a

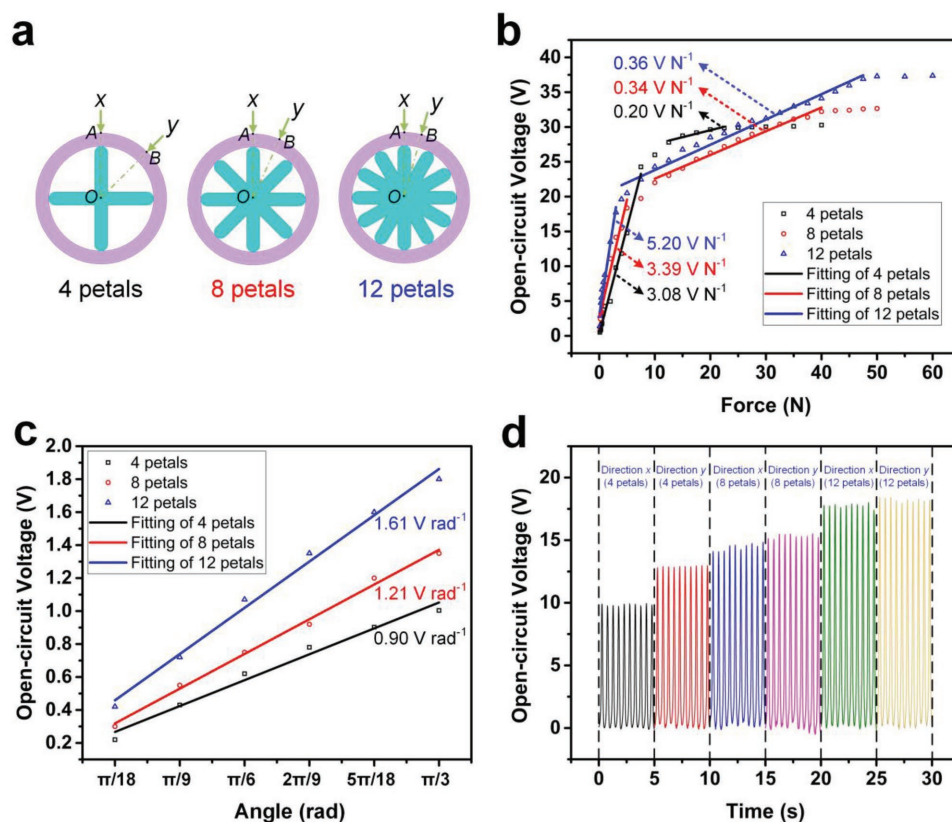


Figure 2. Electrical outputs of the TTEFBSs with different petal numbers under pressing and bending. a) Illustrations of the TTEFBSs with different petal numbers. b) Open-circuit voltages under various pressing forces. c) Open-circuit voltages under various bending angles. d) Open-circuit voltages under different pressing directions with a constant pressing force of 3 N.

range of 0.1–3 N and 0.36 V N^{-1} in a range of 4–47.5 N), compared with that of a triboelectric tactile sensor (0.028 V N^{-1} in a range 40–140 N)^[53] or a force sensor based on capacitive (8.28, 4.53, and 2.97 N^{-1} in unites of relative capacitance, in ranges of 0.032–0.13, 0.13–0.26, and 0.26–0.64 N, respectively).^[54] Furthermore, we tested the electrical outputs under various bending angles. The concrete time profiles of open-circuit voltages and short-circuit currents are presented in Figure S5 in the Supporting Information. In Figure 2c, as the bending angle increases, the output voltage among the three TTEFBSs rises. This increasing behavior can be attributed to the increase of the contact area with the increasing bending angle. Furthermore, the TTEFBS with twelve petals has the highest sensitivity (1.61 V rad^{-1}) with excellent linearity ($R^2 = 0.992$). Additionally, the I_{SC} values among the TTEFBSs with various pressing forces and bending angles (Figure S6a,b, Supporting Information) indicate similar trends as the V_{OC} measurements. At last, we investigated the relationship between the output and pressing direction by measuring the outputs of the TTEFBSs with the two directions x and y under a constant pressing force of 3 N, as diagramed in Figure 2d. The TTEFBS with twelve petals shows the smallest variations of V_{OC} with the pressing direction, and the variations in I_{SC} are similar to those in V_{OC} (Figure S6c, Supporting Information), which indicates the output of the TTEFBS with twelve petals is independent of the pressing direction. Hence, the TTEFBS with twelve petals is optimal for application in the force and bend sensing because

it has the greatest sensitivities, and shows stable performance along random pressing directions.

Since the mechanical stimulation from the environment is irregular and varies in frequency, it is essential to study the dependence of TTEFBS's output on frequency. Thus, the voltage and current responses of the TTEFBS with twelve petals were tested at a constant cyclic pressing force of $\approx 5.0 \text{ N}$ over a range of frequencies from 1 to 10 Hz. As shown in Figure 3a,b, the output voltage V_{OC} is $\approx 20.5 \text{ V}$, and remains almost unchanged at various frequencies. The reason for this is that the open-circuit condition does not involve the dynamic process of charge transfer.^[55] In contrast to the V_{OC} , the I_{SC} increases with frequency, rising from $0.476 \mu\text{A}$ at 1 Hz to $1.603 \mu\text{A}$ at 10 Hz. This is because the increased deformation rate results in a fast flow rate of charges.^[55] Note that the V_{OC} relates to the applied force but is hardly affected by the triggered frequency, indicating that V_{OC} is a reliable parameter that could be used for force sensing.

Furthermore, a step was taken to examine the response time of the TTEFBS to external forces. A real-time measurement of the applied force with its corresponding output voltage is plotted in Figure 3c. From the comparison of the force curve and the voltage curve for the loading and unloading process of the external force, it is estimated that both the response time and relaxation time are $< 6 \text{ ms}$. This prompt response justifies the practicability of the TTEFBS for detecting dynamic force, which is of great importance for applications of landslide

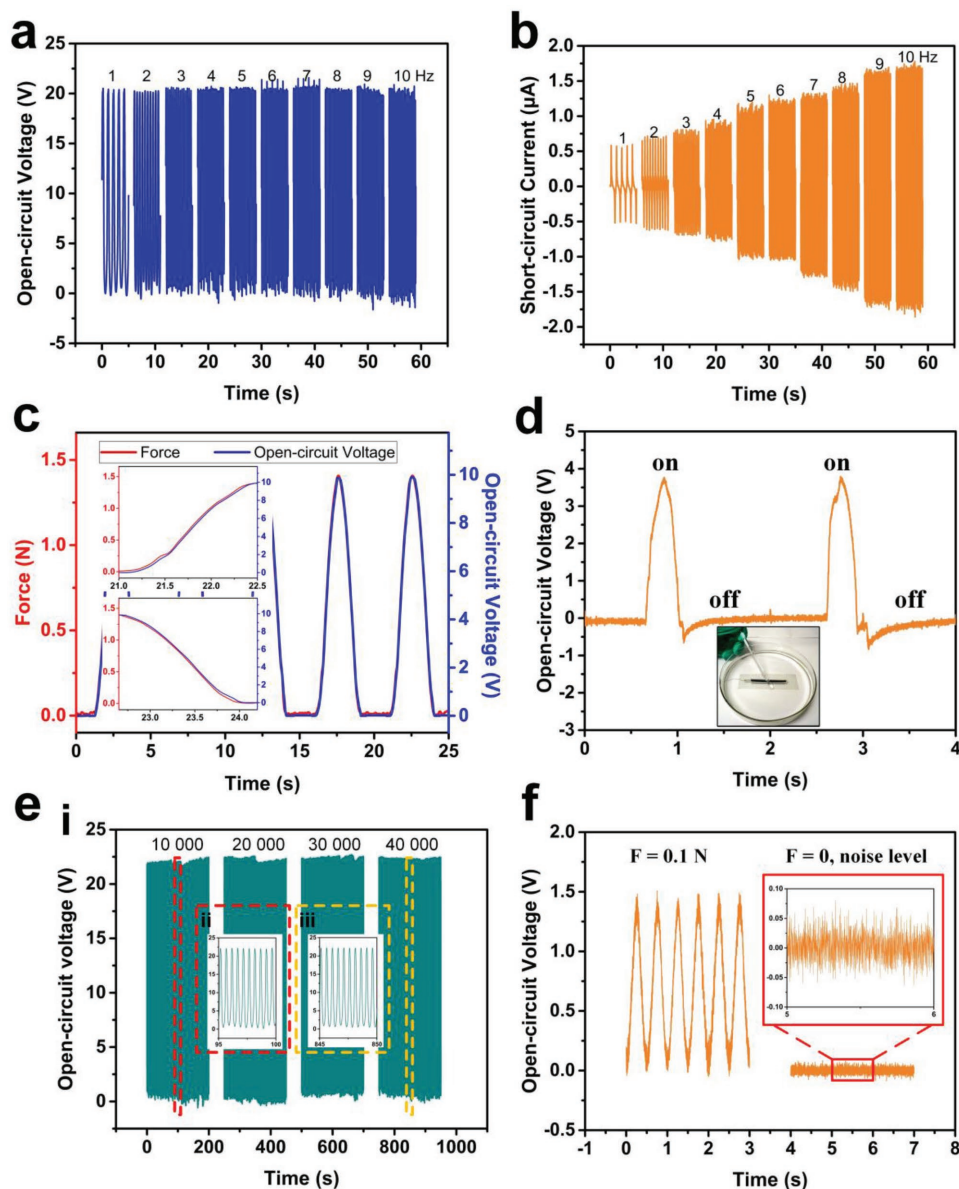


Figure 3. Characterization results of the TTEFBS. a) Open-circuit voltages and b) short-circuit currents of the TTEFBS at a constant pressing force of 5 N under various frequencies. c) Comparison of the real-time measurement for both the applied force (red curve) and the V_{OC} (blue curve). Enlarged views of the loading and unloading process in one cycle are respectively elucidated in (up) and (down), which renders a response time of <6 ms. d) Output voltage in water. Inset: photograph of TTEFBS in water. e) Mechanical durability characterization of the sensor. e-i) Open-circuit voltage under a force of 7 N at a frequency of 2 Hz for 40 000 cycles. Enlarged views of ten cycles for e-ii) the first 10 000 cycles and e-iii) the last 10 000 cycles. f) Measurement of the low-end detection limit of the TTEFBS.

monitoring. Additionally, because the outputs of TENGs are easily affected by humidity in moist environments,^[56] we sealed the sensor with an insulated tube with a thickness of 0.2 mm and an outer diameter of 5.5 mm to protect the sensor from humidity and measured its output voltages when setting it in water, as shown in Figure 3d and Movie S1 (Supporting Information). The TTEFBS can reliably detect the manual press and release using a glass rod with small applied forces. In the low-force region of 0.1–3 N, the TTEFBS with twelve petals has a fitting relationship expression of V_{OC} and force (F): $V_{OC} = 5.2F + 2.89$ (V). Taking the $V_{OC} \approx 3.79$ V, the applied force $F \approx 0.173$ N. The

results reveal that the TTEFBS can work steadily in water, further indicating that the sensor can be employed in real moist environmental conditions.

Moreover, the stability of the TTEFBS was examined through continuously loading and unloading under a constant force (≈ 7 N) at a frequency of 2 Hz for 40 000 cycles. The voltage and current responses were measured after every 10 000 cycles, during which 400 cycles were recorded, as exhibited in Figure 3e. The voltage response merely shows a minor decay of $\approx 4.6\%$, after 40 000 cycles. A little decay of $\approx 3.1\%$ is found in the current response, as displayed in

Figure S6d in the Supporting Information. The V_{OC} and I_{SC} of the TTEFBS under a bending angle of $\pi/6$ at a frequency of 2 Hz for 40 000 cycles are given in Figure S6e–f in the Supporting Information, with decay of $\approx 4.7\%$ and $\approx 4.3\%$, respectively. Hence, the stability of the TTEFBS is confirmed because of its robustness.

More importantly, the force sensing limit of the TTEFBS with twelve petals is examined by comparing the voltage signals of both a gentle force (0.1 N) and the corresponding noise level, as shown in Figure 3f. The low-end detection limit (F_0) can be calculated by the following equation

$$F_0 = \frac{F}{V_{OC}/V_{OC,noise}} = \frac{0.1}{1.4/0.1} \text{N} \approx 7 \text{mN} \quad (1)$$

Hence, the low-end detection limit of the TTEFBS with twelve petals is merely 7 mN, elaborating the high sensitivity of the TTEFBS.

Because there exist a great number of slopes alongside road networks, early warning for landslide incidents occurring along roads, highways, and railways is a vital safety practice for human lives, as schematically depicted in Figure 4a. In general, large-scale slope protection fences made up of steel cables are widely used to intercept falling rocks for protecting roads, railways, and buildings under steep slopes. When rocks tumble along the slope and collide with the protection fence, they will lead to deformations of the steel cables at the points of collision. The deformations suggest that the protection fences can give available information for analyzing and judging the occurrence of rockfalls. The deformation of the steel cable can lead to the bending of the TTEFBS when the TTEFBS is arranged on the steel cable, as indicated in Figure S7 in the Supporting Information. As demonstrated in Figure 4b, five TTEFBSs, labeled as sensors 1–5 and composed as an array, are arranged and installed at various positions on a protection fence with a $1 \text{ m} \times 1 \text{ m}$ grid, so as to detect the deformations during

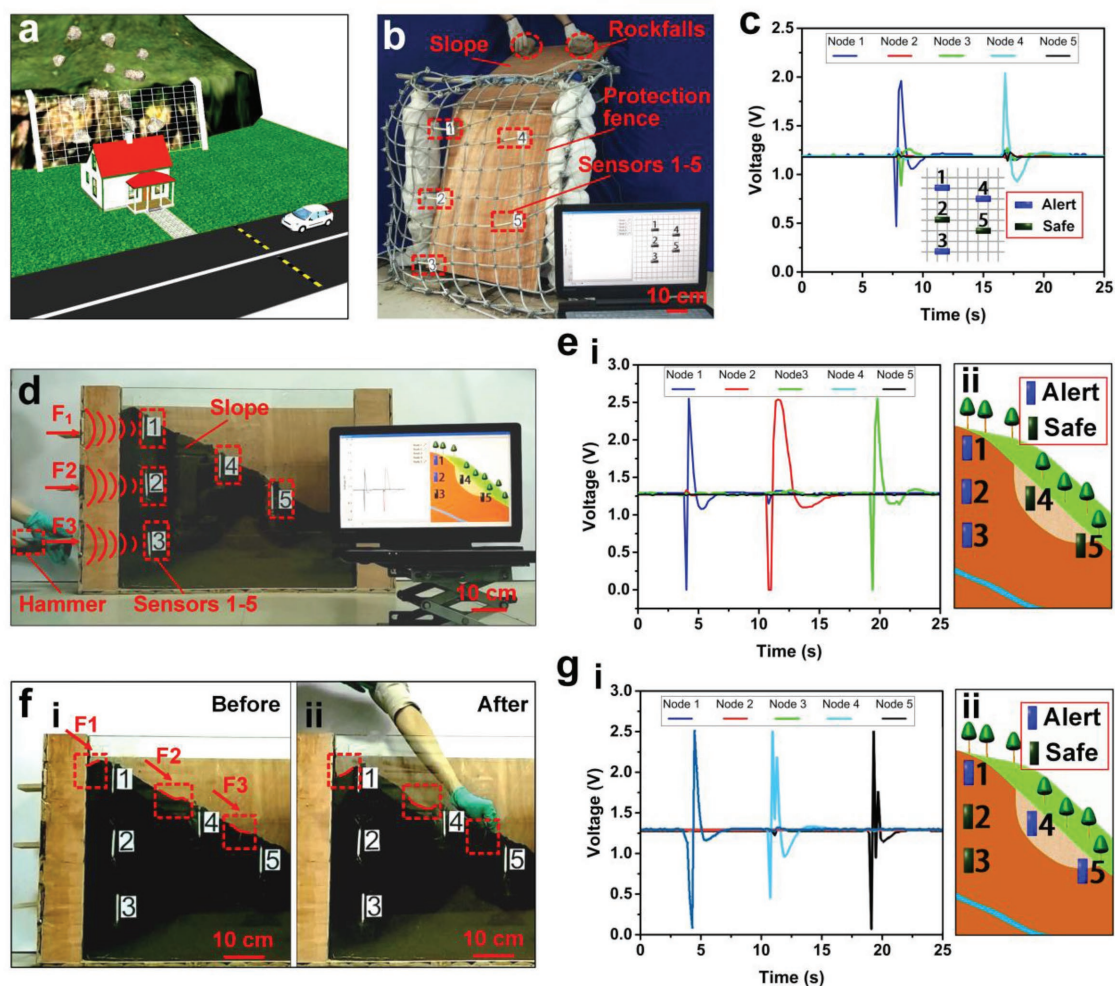


Figure 4. Rockfall detection, deep-seated, and superficial landslides monitoring based on TTEFBSs array. a) Schematic diagram of rockfall detection, deep-seated, and superficial landslides monitoring. b) Experimental setup for rockfall detection (scale bar, 10 cm). c) Acquired output voltage signals in the rockfall detection. Inset: alarm interface. d) Experimental setup for deep-seated landslide monitoring (scale bar, 10 cm). e-i) Acquired output voltage signals and e-ii) alarm interface in deep-seated landslide monitoring. f) Experimental setup for superficial landslide monitoring f-i) before and f-ii) after stirring the superficial soil layers (scale bar, 10 cm). g-i) Acquired output voltage signals and g-ii) alarm interface in superficial landslide monitoring.

rockfalls. White insulated tube with a thickness of 0.2 mm and an outer diameter of 5.5 mm is employed to seal TTEFBSSs to protect them from moisture and dust. As demonstrated in Movie S2 in the Supporting Information, when two rocks are released, they tumble along the slope and finally impact the protection fence at the regions where sensors 1, 3, and 4 are located. As revealed in Figure 4c, the sensors 1, 3, and 4 show voltage variations of 1.49, 0.37, and 1.11 V, respectively, thus giving the alarm (Inset of Figure 4c). This demonstration provides strong evidence that the TTEFBSSs can not only detect the deformations of steel cables, but can also locate rockfall incident sites during rockfall monitoring. Furthermore, deep-seated slope failures and superficial landslides often occur on steep or loose slopes in mountainous regions. Therefore, we designed a soil box with dimensions of 0.90 m × 0.22 m × 0.60 m, in which loose soils of ≈91 kg were loaded, so as to form a slope with a gradient of ≈27°. Three TTEFBSSs, labeled 1, 4, and 5, are arranged in the superficial layer along the slope, while two TTEFBSSs, labeled 2 and 3, are buried at different depths in the soil, as indicated in Figure 4d. Three planks are implanted on the left side of the soil box, and the horizontal separations between the planks and the sensors 1, 2, and 3 are all ≈18 cm. When successively knocking on the planks with a hammer to simulate the deep-seated slope failures, the output voltage variations acquired by the sensors 1, 2, and 3 are all ≈2.55 V, while those of the sensors 4 and 5 are ≈0 V (Figure 4e-i). According to the voltage variations, the alarm raises (Figure 4e-ii) and the deep-seated slope failures are detected and located by the system, as demonstrated in Movie S3 in the Supporting Information. In addition, to demonstrate the feasible application to superficial landslide monitoring, we successively stirred the superficial soil layers near the sensors 1, 4, and 5, as shown in Figure 4f-i, which led to the sliding of the superficial soil layer, as shown in Figure 4f-ii and highlighted in red lines. The voltage variations of the sensors 1, 4, and 5 reach 2.45, 2.04, and 2.42 V, respectively, whereas the signals from the sensors 2 and 3 remain unchanged (Figure 4g-i), indicating that the TTEFBSSs are able to detect the force variations toward them caused by the superficial sliding. Alarms are raised in sensors 1, 4, and 5 successively in the alarm interface (Figure 4g-ii). A visualized demonstration of the TTEFBSSs in superficial landslide monitoring is presented in Movie S4 in the Supporting Information. These two demonstrations indicate that the TTEFBSS is capable of being applied for monitoring deep-seated and superficial landslides. For the TTEFBSSs array, each TTEFBSS connects a signal acquisition channel. In safe state, the signals from TTEFBSSs remain unchanged. When deep-seated slope failures, superficial landslides, or rockfalls occur around the TTEFBSS, the TTEFBSS can generate voltage signal. If the voltage signals from the distributed TTEFBSSs are larger than the threshold, it is determined that the landslides occur near the TTEFBSSs. Hence, according to the voltage variations, the alarm raises and the landslides are detected and located.

To establish a self-powered landslide monitoring system, we designed a zigzag-structured triboelectric nanogenerator (Z-TENG) for scavenging ambient mechanical energy as a power source. As schemed in Figure 5a, the Z-TENG consists of five TENG units in series, and its fabrication is described in the experimental section. The full cycle of the electricity generation process for each TENG can be seen in Figure S8 in the Supporting

Information. The Z-TENG is anchored in a deceleration strip for scavenging energy from moving cars, as shown in Figure 5b. As demonstrated in Figure 5c and Movie S5 (Supporting Information), the Z-TENG directly lights 992 commercial light-emitting diodes (LEDs) when a car passes forth and back over the deceleration strip. The peak values of V_{OC} and I_{SC} reach ≈2058 V and ≈154 μA, respectively, as plotted in Figure 5d–e. This high-output performance of the Z-TENG in harvesting energy from moving cars indicates its potential as a power source. As presented in Figure 5f, the generated electricity can be stored directly as electrochemical energy by storage elements such as batteries and capacitors that can provide power to other circuits, such as a signal processing circuit.^[57] By combining the Z-TENG with the TTEFBSSs array and signal processing circuit, a self-powered wireless and distributed landslide monitoring system for rockfall detection and deep-seated and superficial landslides monitoring can be developed. The TTEFBSSs array could be spatially distributed to acquire real-time information from protection fences and slopes. A wireless transmitter in signal processing circuit can send out the signals from the TTEFBSSs array remotely. It is worth mentioning that, data transmission distance is ≈15 m through Bluetooth in lab environment; while in outdoor environment, by employing general packet radio service (GPRS), the data transmission distance between the wireless transmitter and the control terminal is not limited under the case of great communication signals, which meets the requirement of the practical application. Such a self-powered wireless and distributed landslide monitoring system enables evacuation of vulnerable people and allows timely repair and maintenance of critical infrastructures.

3. Conclusion

In summary, we present an unusual design of TTEFBSSs for force and bend sensing in landslide monitoring. The self-powered TTEFBSS has the sensitivities of 5.20 V N⁻¹ under pressing and 1.61 V rad⁻¹ under bending, fast response/relaxation time of <6 ms, and long-term stability/reliability for 40 000 cycles, as well as stability in water. Because of the superior performance of the TTEFBSS, multiple TTEFBSSs are integrated into an array for landslide monitoring. Additionally, a Z-TENG is successfully fabricated for scavenging energy from cars on roads, showing its potential application as power sources in self-powered, effective, and real-time landslide monitoring system. Such a monitoring system has great potential for providing early warning of landslide disasters, and thus can reduce the numbers of casualties and economic losses. This work will further inspire rapid progress of TENG in applications of wireless, distributed sensing, and environmental/infrastructure monitoring.

4. Experimental Section

Fabrication of a TTEFBSS: The die with timbo-like inner cavity was made through wire-electrode cutting method to fabricate the mold for polydimethylsiloxane (PDMS) casting. The base and curing agent was evenly mixed in a mass ratio of 10: 1. Next, the mixture of PDMS was poured into the cavity of the die. Then the die with the mixture of PDMS was set in the drying oven at a constant temperature of 100 °C for 90 min. After curing, the PDMS mode was peeled off from the inner

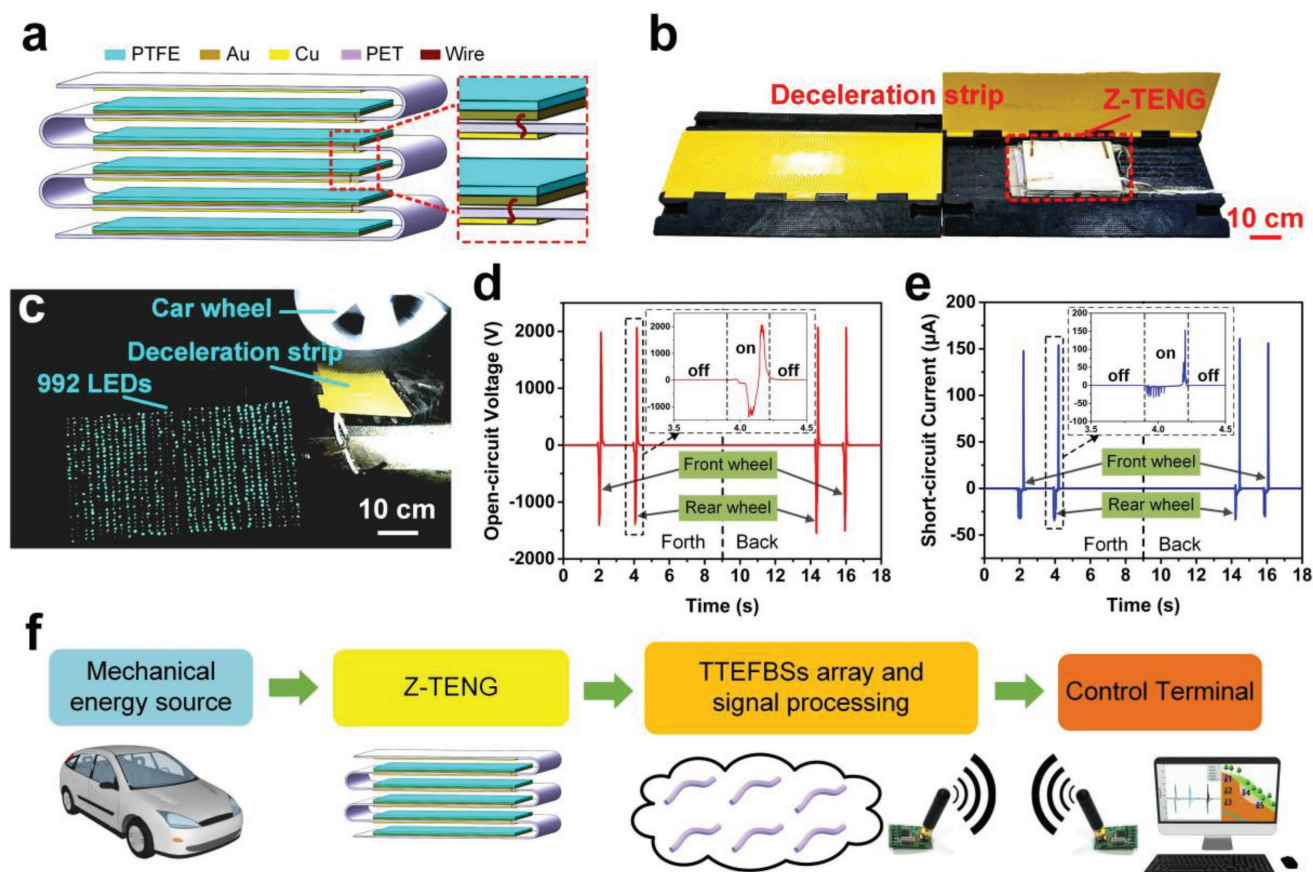


Figure 5. Self-powered TENG-based landslide monitoring system. a) Zigzag-Structured design of the TENG. b) Photograph of the Z-TENG in a deceleration strip (scale bar, 10 cm). c) Z-TENG used as a power source to light 992 commercial LEDs (scale bar, 10 cm). d) Open-circuit voltage and e) short-circuit current when the car passed forth and back over the deceleration strip. f) Diagram of self-powered landslide monitoring system.

cavity of the die. After that, the processed PDMS core was deposited with a 100 μm thick carbon electrode on its outer surface. Finally, the whole inner core was suitably installed in a silicon rubber tube with inner and outer diameters of 4 and 5 mm, respectively.

Fabrication of Nanowires on PTFE Surface: First, a piece of 25 μm thick polytetrafluoroethylene (PTFE) film was rinsed with menthol, isopropyl alcohol, and deionized water. Then, the inductively coupled plasma (ICP) reactive ion etching was employed to fabricate the aligned nanowires on PTFE surface. O_2 , Ar, and CF_4 gases were injected into the ICP chamber at a flow ratio of 10.0, 15.0, and 30.0 sccm, respectively. A power source of 400 W was applied to produce a large density of plasma. Another power source of 100 W was used in order to accelerate the plasma ions. The nanowires on PTFE surface were obtained after an etching process for 60 s.

Fabrication of a Z-TENG: The Z-TENG was made up of five TENG units in series. In each unit, a 25 μm thick polytetrafluoroethylene (PTFE) film with a 100 nm thick Au back electrode was cut into a rectangle with dimensions of 16 cm \times 20 cm, and was attached to a side of a 1 mm thick polyethylene terephthalate (PET) layer, and a 30 μm thick Cu foil was attached to the opposite side of the PET layer.

Experimental Setup for Electrical Measurements: The TTEFBS was mounted on an electrodynamic shaker (Labworks ET-139) powered by an amplified sinusoidal wave from a function signal generator (Tektronix AFG3021) and power amplifier (LabworkPa-13). A digital force gauge (DSM-50) was fixed over the TTEFBS to measure and control the pressing force applied to the TTEFBS. The lead wire from the TTEFBS was connected to an electrometer (Keithley Model 6514) to measure the outputs of the TTEFBS. The computer stored the measured force and the outputs of the TTEFBS.

Supporting Information

Supporting Information is available from the Wiley Online Library or from the author.

Acknowledgements

This work was supported by National Key R&D Program of China (2016YFC0801200), and the National Natural Science Foundation of China (No. 51675069).

Conflict of Interest

The authors declare no conflict of interest.

Keywords

landslide monitoring, self-powered system, timbo-like structure, triboelectric nanogenerator

Received: May 3, 2018
Revised: June 11, 2018
Published online:

- [1] W. H. Schulz, J. W. Kean, G. Wang, *Nat. Geosci.* **2009**, *2*, 863.
- [2] D. Petley, *Geology* **2012**, *40*, 927.
- [3] A. C. Seijmonsbergen, L. W. S. de Graaff, *Nat. Hazards Earth Sys.* **2006**, *6*, 185.
- [4] F. Weirich, L. Blesius, *Geomorphology* **2007**, *87*, 352.
- [5] S. C. Stiros, C. Vichas, C. Skourtis, *J. Surv. Eng.-Asce.* **2004**, *130*, 156.
- [6] C. Squarzon, C. Delacourt, P. Allemand, *Eng. Geol.* **2005**, *79*, 215.
- [7] F. Guzzetti, A. C. Mondini, M. Cardinali, F. Fiorucci, M. Santangelo, K.-T. Chang, *Earth-Sci. Rev.* **2012**, *112*, 42.
- [8] J.-C. Du, H.-C. Teng, *Automat. Constr.* **2007**, *16*, 657.
- [9] P. Farina, D. Colombo, A. Fumagalli, F. Marks, S. Moretti, *Eng. Geol.* **2006**, *88*, 200.
- [10] K. A. Razak, M. W. Straatsma, C. J. van Westen, J. P. Malet, S. M. de Jong, *Geomorphology* **2011**, *126*, 186.
- [11] M. Van Den Eeckhaut, J. Poesen, G. Verstraeten, V. Vanacker, J. Nyssen, J. Moeyersons, L. P. H. van Beek, L. Vandekerckhove, *Earth Surf. Processes Landforms* **2007**, *32*, 754.
- [12] A. Perrone, V. Lapenna, S. Piscitelli, *Earth-Sci. Rev.* **2014**, *135*, 65.
- [13] A. Lalague, M. A. Lebens, I. Hoff, E. Grov, *Rock Mech. Rock Eng.* **2016**, *49*, 2811.
- [14] C.-Y. Hong, Y.-F. Zhang, G.-W. Li, M.-X. Zhang, Z.-X. Liu, *Sens. Actuators, A* **2017**, *258*, 131.
- [15] F.-R. Fan, Z.-Q. Tian, Z. Lin Wang, *Nano Energy* **2012**, *1*, 328.
- [16] Z. L. Wang, J. Chen, L. Lin, *Energy Environ. Sci.* **2015**, *8*, 2250.
- [17] J. Yang, J. Chen, Y. Yang, H. Zhang, W. Yang, P. Bai, Y. Su, Z. L. Wang, *Adv. Energy Mater.* **2014**, *4*, 1301322.
- [18] Y. Hu, J. Yang, Q. Jing, S. Niu, W. Wu, Z. L. Wang, *ACS Nano* **2013**, *7*, 10424.
- [19] X. Wang, S. Niu, F. Yi, Y. Yin, C. Hao, K. Dai, Y. Zhang, Z. You, Z. L. Wang, *ACS Nano* **2017**, *11*, 1728.
- [20] L.-B. Huang, G. Bai, M.-C. Wong, Z. Yang, W. Xu, J. Hao, *Adv. Mater.* **2016**, *28*, 2744.
- [21] S. Kim, M. K. Gupta, K. Y. Lee, A. Sohn, T. Y. Kim, K.-S. Shin, D. Kim, S. K. Kim, K. H. Lee, H.-J. Shin, D.-W. Kim, S.-W. Kim, *Adv. Mater.* **2014**, *26*, 3918.
- [22] D. Bhatia, W. Kim, S. Lee, S. W. Kim, D. Choi, *Nano Energy* **2017**, *33*, 515.
- [23] J. H. Lee, R. Hinchet, S. K. Kim, S. Kim, S.-W. Kim, *Energy Environ. Sci.* **2015**, *8*, 3605.
- [24] L. Liu, W. Tang, B. Chen, C. Deng, W. Zhong, X. Cao, Z. L. Wang, *Adv. Mater. Technol.* **2018**, *3*, 1700209.
- [25] J. Yang, J. Chen, Y. Liu, W. Yang, Y. Su, Z. L. Wang, *ACS Nano* **2014**, *8*, 2649.
- [26] X. Fan, J. Chen, J. Yang, P. Bai, Z. Li, Z. L. Wang, *ACS Nano* **2015**, *9*, 4236.
- [27] Y. Bian, T. Jiang, T. Xiao, W. Gong, X. Cao, Z. Wang, Z. L. Wang, *Adv. Mater. Technol.* **2018**, *3*, 1700317.
- [28] J. Bae, J. Lee, S. Kim, J. Ha, B. S. Lee, Y. Park, C. Choong, J. B. Kim, Z. L. Wang, H. Y. Kim, J. J. Park, U. I. Chung, *Nat. Commun.* **2014**, *5*, 4929.
- [29] R. Cao, J. Wang, Y. Xing, W. Song, N. Li, S. Zhao, C. Zhang, C. Li, *Adv. Mater. Technol.* **2018**, *3*, 1700371.
- [30] G. Zhu, Y. Su, P. Bai, J. Chen, Q. Jing, W. Yang, Z. L. Wang, *ACS Nano* **2014**, *8*, 6031.
- [31] G. Cheng, Z.-H. Lin, Z.-I. Du, Z. L. Wang, *ACS Nano* **2014**, *8*, 1932.
- [32] X. N. Wen, W. Q. Yang, Q. S. Jing, Z. L. Wang, *ACS Nano* **2014**, *8*, 7405.
- [33] A. Ahmed, Z. Saadtnia, I. Hassan, Y. Zi, Y. Xi, X. He, J. Zu, Z. L. Wang, *Adv. Energy Mater.* **2017**, *7*, 1601705.
- [34] M.-F. Lin, K. Parida, X. Cheng, P. S. Lee, *Adv. Mater. Technol.* **2017**, *2*, 1600186.
- [35] L. B. Huang, W. Xu, G. X. Bai, M. C. Wong, Z. B. Yang, J. H. Hao, *Nano Energy* **2016**, *30*, 36.
- [36] W. Xu, L. B. Huang, J. H. Hao, *Nano Energy* **2017**, *40*, 399.
- [37] M. Salauddin, H. Cho, J. Y. Park, *Adv. Mater. Technol.* **2018**, *3*, 1700240.
- [38] K. Parida, V. Kumar, J. Wang, V. Bhavanasi, R. Bendi, P. S. Lee, *Adv. Mater.* **2017**, *29*, 1702181.
- [39] P. Vasandani, B. Gattu, J. Wu, Z.-H. Mao, W. Jia, M. Sun, *Adv. Mater. Technol.* **2017**, *2*, 1700014.
- [40] Y. Yin, J. Wang, S. Zhao, W. Fan, X. Zhang, C. Zhang, Y. Xing, C. Li, *Adv. Mater. Technol.* **2018**, *3*, 1700370.
- [41] L. Zhang, Y. Yu, G. P. Eyer, G. Suo, L. A. Kozik, M. Fairbanks, X. Wang, T. L. Andrew, *Adv. Mater. Technol.* **2016**, *1*, 1600147.
- [42] H. Zhang, Y. Yang, Y. Su, J. Chen, C. Hu, Z. Wu, Y. Liu, C. P. Wong, Y. Bando, Z. L. Wang, *Nano Energy* **2013**, *2*, 693.
- [43] Y. Xi, H. Y. Guo, Y. L. Zi, X. G. Li, J. Wang, J. N. Deng, S. M. Li, C. G. Hu, X. Cao, Z. L. Wang, *Adv. Energy Mater.* **2017**, *7*, 1602397.
- [44] B. D. Chen, W. Tang, C. He, T. Jiang, L. Xu, L. P. Zhu, G. Q. Gu, J. Chen, J. J. Shao, J. J. Luo, Z. L. Wang, *Adv. Mater. Technol.* **2018**, *3*, 1700229.
- [45] B. Zhang, L. Zhang, W. Deng, L. Jin, F. Chun, H. Pan, B. Gu, H. Zhang, Z. Lv, W. Yang, Z. L. Wang, *ACS Nano* **2017**, *11*, 7440.
- [46] S. Wang, L. Lin, Z. L. Wang, *Nano Energy* **2015**, *11*, 436.
- [47] G. Zhu, W. Q. Yang, T. Zhang, Q. Jing, J. Chen, Y. S. Zhou, P. Bai, Z. L. Wang, *Nano Lett.* **2014**, *14*, 3208.
- [48] J. Yang, J. Chen, Y. Su, Q. Jing, Z. Li, F. Yi, X. Wen, Z. Wang, Z. L. Wang, *Adv. Mater.* **2015**, *27*, 1316.
- [49] W. Xu, L.-B. Huang, M.-C. Wong, L. Chen, G. Bai, J. Hao, *Adv. Energy Mater.* **2017**, *7*, 1601529.
- [50] K. Parida, V. Bhavanasi, V. Kumar, R. Bendi, P. S. Lee, *Nano Res.* **2017**, *10*, 3557.
- [51] H. Zhang, Y. Yang, Y. Su, J. Chen, K. Adams, S. Lee, C. Hu, Z. L. Wang, *Adv. Funct. Mater.* **2014**, *24*, 1401.
- [52] P. Bai, G. Zhu, Q. Jing, Y. Wu, J. Yang, J. Chen, J. Ma, G. Zhang, Z. L. Wang, *Nano Energy* **2015**, *12*, 278.
- [53] T. Li, J. Zou, F. Xing, M. Zhang, X. Cao, N. Wang, Z. L. Wang, *ACS Nano* **2017**, *11*, 3950.
- [54] L. Viry, A. Levi, M. Totaro, A. Mondini, V. Mattoli, B. Mazzolai, L. Beccai, *Adv. Mater.* **2014**, *26*, 2659.
- [55] S. Wang, L. Lin, Z. L. Wang, *Nano Lett.* **2012**, *12*, 6339.
- [56] L. Zhang, B. Zhang, J. Chen, L. Jin, W. Deng, J. Tang, H. Zhang, H. Pan, M. Zhu, W. Yang, Z. L. Wang, *Adv. Mater.* **2016**, *28*, 1650.
- [57] Z. L. Wang, *Mater. Today* **2017**, *20*, 74.